



Cite as

Nano-Micro Lett.
(2020) 12:87Received: 15 January 2020
Accepted: 28 February 2020
© The Author(s) 2020

Interfacial Voids Trigger Carbon-Based, All-Inorganic CsPbIBr₂ Perovskite Solar Cells with Photovoltage Exceeding 1.33 V

Weidong Zhu¹ ✉, Zeyang Zhang¹, Dandan Chen², Wenming Chai¹, Dazheng Chen¹, Jincheng Zhang¹, Chunfu Zhang¹ ✉, Yue Hao¹

Weidong Zhu and Zeyang Zhang have contributed equally to this work.

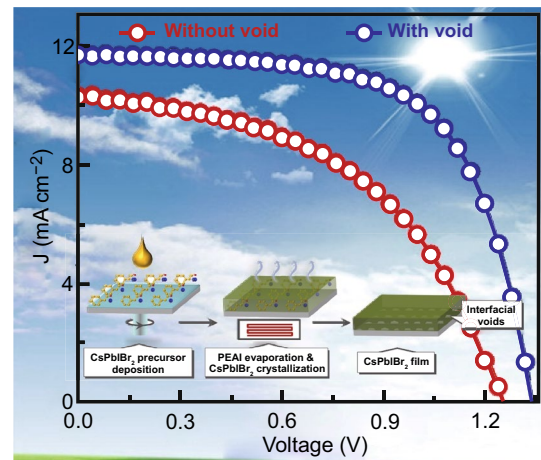
✉ Weidong Zhu, wdzhu@xidian.edu.cn; Chunfu Zhang, cfzhang@xidian.edu.cn

¹ State Key Discipline Laboratory of Wide Band Gap Semiconductor Technology and Shaanxi Joint Key Laboratory of Graphene, School of Microelectronics, Xidian University, Xi'an 710071, People's Republic of China² College of Science, Xi'an Shiyong University, Xi'an 710065, Shaanxi, People's Republic of China

HIGHLIGHTS

- A novel interface design of producing interfacial voids is proposed for CsPbIBr₂ perovskite solar cells (PSCs), which is free of any extra modification layer.
- Interfacial voids improve absorption of CsPbIBr₂ film, reduce saturation current density, and enlarge built-in potential of the PSCs.
- The PSC yields a superior efficiency of 10.20% with a record-high photovoltage of 1.338 V.

ABSTRACT A novel interface design is proposed for carbon-based, all-inorganic CsPbIBr₂ perovskite solar cells (PSCs) by introducing interfacial voids between TiO₂ electron transport layer and CsPbIBr₂ absorber. Compared with the general interfacial engineering strategies, this design exempts any extra modification layer in final PSC. More importantly, the interfacial voids produced by thermal decomposition of 2-phenylethylammonium iodide trigger three beneficial effects. First, they promote the light scattering in CsPbIBr₂ film and thereby boost absorption ability of the resulting CsPbIBr₂ PSCs. Second, they suppress recombination of charge carriers and thus reduce dark saturation current density (J_0) of the PSCs. Third, interfacial voids enlarge built-in potential (V_{bi}) of the PSCs, awarding increased driving force for dissociating photo-generated charge carriers. Consequently, the PSC yields the optimized efficiency of 10.20% coupled with an open-circuit voltage (V_{oc}) of 1.338 V. The V_{oc} achieved herein represents the best value among CsPbIBr₂ PSCs reported earlier. Meanwhile, the non-encapsulated PSCs exhibit an excellent stability against light, thermal, and humidity stresses, since it remains ~97% or ~94% of its initial efficiency after being heated at 85 °C for 12 h or stored in ambient atmosphere with relative humidity of 30–40% for 60 days, respectively.

KEYWORDS All-inorganic perovskite solar cells; CsPbIBr₂; Photovoltage; Interfacial engineering; Stability

1 Introduction

Organic–inorganic hybrid perovskite semiconductors have emerged as promising absorber materials for solar cells that are known as perovskite solar cells (PSCs), owing to their excellent optoelectronic properties, low cost, and versatile low-temperature processability of thin films [1–4]. Furthermore, the certified power conversion efficiency (PCE) of PSCs has reached up to 25.2% [5], approaching that of commercial crystalline silicon solar cells. However, the poor stability of organic–inorganic hybrid perovskite films under thermal, humidity, and light stresses brings a severe reliability issue to PSCs [3, 4, 6]. In addition, most of high-efficiency PSCs generally contain expensive and unstable organic hole transport layers (HTLs) coupled with noble metal electrodes. These functional films not only aggravate the instability problem but also burden the production cost of corresponding PSCs [3, 6, 7]. Hence, there is a growing attention to carbon-based, all-inorganic PSCs that avoid use of any HTLs and noble metal electrodes, in view of their multiply superiorities including upgraded stability, cost-effectiveness, and facile fabrication [7–11].

Currently, the absorber materials explored for carbon-based, all-inorganic PSCs largely include CsPbI₃ [12, 13], CsPbI₂Br [14–16], CsPbIBr₂ [8, 17–20], and CsPbBr₃ [7, 9, 21–23]. Among them, CsPbIBr₂ holds the relatively well-balanced characters of bandgap and phase stability [8, 17–19, 24, 25]. Meanwhile, CsPbIBr₂ is also applicable to build photovoltaic windows [26], semitransparent solar cells [27], water splitting systems [28], and tandem solar cells in conjunction with the state-of-the-art photovoltaic technologies [11]. Nevertheless, the PCEs of carbon-based, all-inorganic CsPbIBr₂ PSCs are still far from their theoretical level [29, 30], and even lag behind that of the ones based on other analogs [13, 15, 23]. This dilemma can be largely attributed to their inferior open-circuit voltage (V_{oc}) and fill factor (FF) values, which are eventually caused by the serious non-radiative recombination within CsPbIBr₂ films and interfacial recombination in the PSCs.

To solve the above obstacles, great efforts have been dedicated in improving the quality of CsPbIBr₂ films, targeting to suppress non-radiative recombination of charge carriers, by crystallization engineering or heteroatom replacement on Cs site or Pb site [19, 20, 25, 31]. For example, our previous work [19] demonstrated that modification of general

one-step method with an intermolecular exchange reaction could produce a pinhole-free CsPbIBr₂ film composed of micro-sized, [100] preferential grains, which finally enabled an optimized PCE of 9.16%. More recently, it was reported that Ba(II) doping could boost the grain sizes and crystallinity of CsPbIBr₂ film, bringing out reduced trap states and suppressed non-radiative recombination. As a result, the PCE of corresponding PSC was boosted from 8.40 to 10.51% [31].

Interfacial modification with extra functional materials has been attempted to weaken interfacial recombination of charge carriers and therefore improve the PCEs of CsPbIBr₂ PSCs [17, 18, 30, 32]. For example, the innovative modification of TiO₂ electron transport layer (ETL) with CsBr or SmBr₃ could strikingly improve the PSC's PCE to over 10% coupled with desirable FF of ~0.70, which represents the highest PCE among CsPbIBr₂ PSCs reported to date [18, 30]. Guo et al. [17] reported that surficial passivation of SnO₂ ETL could enable the CsPbIBr₂ PSCs with a record-high V_{oc} of 1.31 V in spite of its low PCE of 2.06%. Clearly, these progresses verify the considerable feasibility of interfacial modification strategy in overcoming the obstacle faced by carbon-based, all-inorganic CsPbIBr₂ PSCs. However, the extra interfacial modifiers inevitably complex the configuration of CsPbIBr₂ PSCs and thus bring some new parasitic issues. For example, the modifiers multiply the interfaces of CsPbIBr₂ PSCs, leading to an increased degradation risk [3, 33, 34]. Meanwhile, they will also alter the crystallization dynamics of atop CsPbIBr₂ films [35, 36], which brings a new challenge to prepare high-quality CsPbIBr₂ film. Thus, it is highly desired to develop more feasible interfacial engineering strategy to boost interfacial kinetics of charge carriers in carbon-based, all-inorganic CsPbIBr₂ PSCs, thereby boosting its V_{oc} and FF as well as PCE.

In this study, we propose an interfacial engineering strategy for carbon-based, all-inorganic CsPbIBr₂ PSCs by making interfacial voids between TiO₂ ETL and CsPbIBr₂ film. This strategy avoids introducing any extra modification layer in ultimate PSCs compared with the conventional ones. Further, we reveal that the interfacial voids can stimulate enhanced absorption, decreased interfacial recombination of charge carriers, as well as enlarged built-in potential (V_{bi}) in resulting CsPbIBr₂ PSCs. Hence, the optimized one yields the outstanding PCE of 10.20% coupled with a high V_{oc} of 1.338 V, a FF of 0.65, and a short-circuit current density (J_{sc}) of 11.73 mA cm⁻². The PCE is beyond nearly most of

CsPbIBr₂-based cells reported earlier, and particularly the V_{oc} represents the highest level among them. Moreover, the PSC exhibits excellent photo-stability as well as long-term stability against thermal and humidity stresses.

2 Experimental Section

2.1 Materials and Reagents

Patterned FTO glass substrates (Pilkington, TEC-8, $8 \Omega \text{ sq}^{-1}$) were supplied by Yingkou OPV Tech New Energy Co., Ltd., China. Conductive carbon paste was bought from Shanghai MaterWin New Materials Co., Ltd., China. Lead bromide (PbBr₂, ultra-dry, 99.999%), cesium iodide (CsI, ultra-dry, 99.998%), and dimethyl sulfoxide (DMSO, anhydrous, 99.8+%), isopropanol (anhydrous, 99.5+%) are received from Alfa-Assar. 2-phenylethylammonium iodide (PEAI, 99.99%) was purchased from Xi'an Polymer Light Technology Co., Ltd., China. All of them are used without further treatment or purification.

2.2 Preparation of PEAI-Loaded FTO/TiO₂ Substrate

Firstly, patterned FTO glass with size $2 \times 2.5 \text{ cm}^2$ was washed with detergent, ultrapure water, acetone, and ethanol in an ultrasonic cleaner successively. Next, TiO₂ sol was spin coated onto the FTO glass at 3500 rpm for 30 s. After being annealed at 500 °C for 60 min in ambient air, the FTO/TiO₂ substrate was achieved. Finally, 100 μL 3 mg mL⁻¹ PEAI in isometric deionized water and isopropanol was spin-coated on the substrate at 3500 rpm for 60 s and baked at 80 °C for 5 min in ambient air in order to load PEAI species onto FTO/TiO₂ substrate.

2.3 Deposition of CsPbIBr₂ Film

CsPbIBr₂ precursor (1.0 M) was firstly prepared by dissolving 370.0 mg PbBr₂ and 260.0 mg CsI in 1 mL DMSO at room temperature with vigorously stirring. Then, the PEAI-loaded FTO/TiO₂ substrate was transferred into a N₂-filled glovebox. And, 70 μL CsPbIBr₂ precursor was spin-coated the substrate at 1500 rpm for 20 s and 5000 rpm for 60 s. After the spin-coating process, the sample was annealed at 280 °C for 15 min to form the crystallized CsPbIBr₂ film. For comparison, a CsPbIBr₂ film on FTO/TiO₂ substrate without loading of PEAI species was also prepared according to the same procedures above.

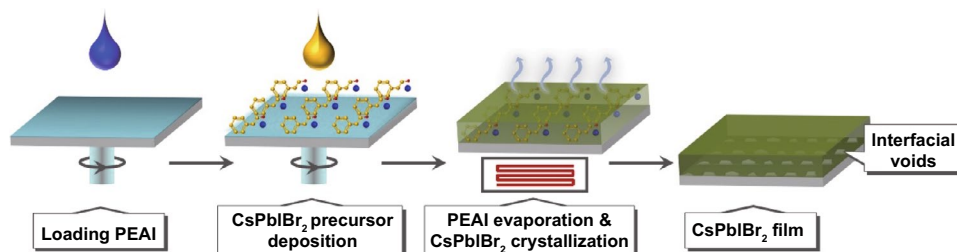
2.4 Fabrication of Carbon-Based, All-Inorganic PSC

Carbon paste with the area of 0.10 cm² was firstly coated on CsPbIBr₂ film by screen-printing method. Then, the sample was heated at 120 °C for 15 min to promote evaporation of solvent of carbon paste. After cooling down naturally to room temperature, the carbon-based, all-inorganic PSC was achieved for further characterizations.

3 Results and Discussion

3.1 Formation Mechanism of CsPbIBr₂ Films with Interfacial Voids

The main preparation procedures of CsPbIBr₂ film with interfacial voids are shown in Scheme 1. To be brief, FTO/TiO₂ substrate was firstly prepared according to the recipe described in our previous work [18, 19]. Then, 2-phenylethylammonium iodide (PEAI, C₆H₅CH₂CH₂NH₃I) in isometric deionized water and isopropanol was deposited on



Scheme 1 Schematic procedures for preparation of CsPbIBr₂ film with interfacial voids

FTO/TiO₂ substrate by spin-coating method, with the aim of loading PEAI species on TiO₂ surface. The successful loading of PEAI can be verified by the scanning electron microscope (SEM) results in Fig. S1. Next, CsPbIBr₂ precursor was spin-coated onto the substrate by one-step spin-coating method. Finally, the sample was annealed at 280 °C for 15 min to promote the crystallization of CsPbIBr₂ grains. It is noted that the release of PEAI species happened simultaneously during this high-temperature annealing stage, as discussed below.

We conducted X-ray photoelectron spectroscopy (XPS) measurement to examine the constituents of obtained CsPbIBr₂ film. For comparison, a same CsPbIBr₂ film that was prepared at a low annealing temperature of 100 °C was also investigated. The reason for adopting this low annealing temperature to prepare the control sample is that it cannot cause the sublimation or decomposition of PEAI molecules, as demonstrated previously [37, 38]. Figure 1a manifests that clear XPS peaks corresponding to Cs, Pb, I, and Br elements appear for the films annealed at either 280 or 100 °C, indicating that they are composed of CsPbIBr₂ materials. However, no any signal corresponding to PEAI species can be

measured from them, even though the FTO/TiO₂ substrate contains PEAI species. The core-level N 1s XPS spectra in Fig. 1b further verify this fact, since the typical N 1s peak of PEAI species is absent [38].

In general, XPS measurement can only reflect surficial composition information of samples. To insight bulk composition of the concerned CsPbIBr₂ films, they were redissolved in situ by *N,N*-dimethylformamide (DMF) solvent and annealed again at 90 °C for 10 min to evaporate the solvent away. As shown in Fig. 1a, after such treatment the additional Sn 3d peaks that originate from FTO/TiO₂ substrate can be detected from both films, indicating the full dissolution of CsPbIBr₂ films by DMF solvent and therefore the possible non-uniform composition distribution in the films or their interfaces is eliminated. In this manner, XPS measurement can be used to study bulk composition of CsPbIBr₂ films reasonably. Once again, as exhibited in Fig. 1b, the N 1s peak located at 401.8 eV can be detected from CsPbIBr₂ film prepared at 100 °C, manifesting the existence of PEAI species in it [37, 38]. By contrast, the peak is still missing in CsPbIBr₂ film prepared at 280 °C, indicating that there is no detectable PEAI species in it indeed. This can

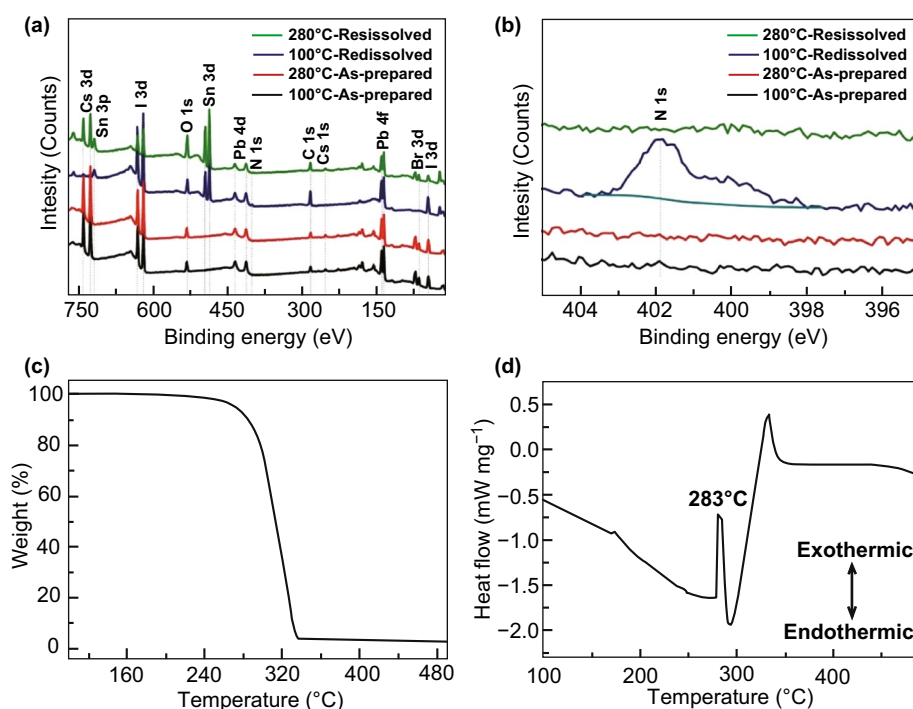


Fig. 1 **a** XPS survey spectra of as-prepared and in situ redissolved CsPbIBr₂ films annealed at 100 °C and 280 °C, **b** corresponding core-level N 1s XPS spectra, **c** TGA heating curve of PEAI powder expressed as weight% as a function of applied temperature, **d** DSC curve of PEAI powder

be also supported by the energy-dispersive spectrometer (EDS) result in Fig. S2. We attribute such phenomenon to the sublimation of PEAI species during the high-temperature annealing stage of CsPbIBr₂ film.

To support our standpoint, thermal property of PEAI powder was investigated by thermogravimetric analysis (TGA) and differential scanning calorimetry (DSC) [39, 40]. The TGA curve in Fig. 1c indicates that PEAI powder undergoes 100% weight loss in one step with the onset temperature of ~185 °C, suggesting that it is sublimated without complex decomposition procedure. This can be supported by the sharp transition step in corresponding differential TGA curve in Fig. S3. Moreover, the endothermic peak at ~283 °C in the DSC curve in Fig. 1d also suggests that the release of PEAI is related to a sublimation process. Thus, the typical sublimation temperature of PEAI powder is estimated to be ~283 °C, which is nearly the same as the annealing temperature of CsPbIBr₂ film adopted in this work. Additionally, it is noted that the DSC measurement was performed on PEAI powder. In the case of within CsPbIBr₂ thin film, a much larger surface-to-volume ratio is provided; therefore, the sublimation temperature could be lowered considerably to below ~283 °C for PEAI. Thus far,

all the above observations provide conclusive evidences that in terms of CsPbIBr₂ film prepared at 280 °C the original PEAI species on FTO/TiO₂ substrate do not reside in its bulk or at its interface, but are sublimated during the thermal annealing stage.

3.2 Morphology Characterization

With this fact in mind, we turned to study the microstructure of CsPbIBr₂ films deposited on FTO/TiO₂ substrates without and with loading of PEAI species. Their top-view SEM images are provided in Fig. 2a, b. Clearly, both films are composed of closely packed crystalline grains without any discernible pinholes. Their grains are featured by dominant triple-junctions grain boundaries with equal vertex angle of 120°, implying that they are in equilibrium state with low internal stress [41, 42]. By contrast, the CsPbIBr₂ film deposited on FTO/TiO₂ substrate loaded with PEAI species exhibits larger grain sizes. The statistical results in Fig. S4 indicate its average grain size of ~576 nm, which is slightly larger than the one deposited on FTO/TiO₂ substrate without loading of PEAI species (~475 nm). It should be noted that the formation of coarsened grains is mainly attributed

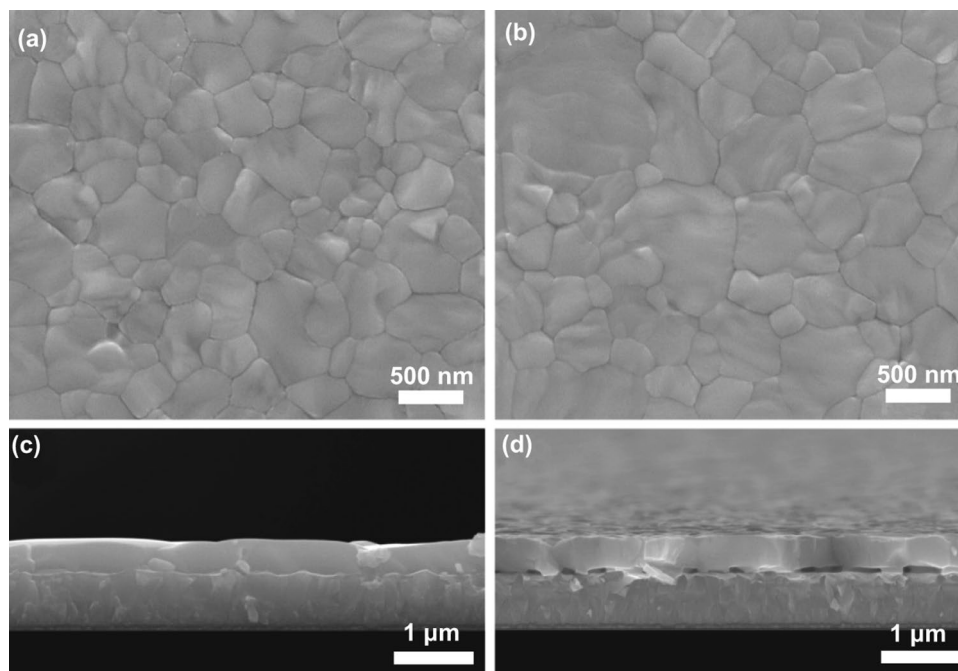


Fig. 2 Top-view and cross-sectional SEM images of CsPbIBr₂ films deposited on FTO/TiO₂ substrates: **a, c** without and **b, d** with loading of PEAI species

to the decreased nucleation density of CsPbIBr₂ grains, as a result of improved non-wetting of CsPbIBr₂ precursor to FTO/TiO₂ substrate induced by PEAI species (Fig. S5) [36, 43], along with the templating effect of PEAI species during the crystallization of CsPbIBr₂ grains.

Figures 2c, d and S6 provide cross-sectional SEM images of the concerned CsPbIBr₂ films. They reveal that the films have a similar thickness of ~400 nm. And, each of individual grains in the films is able to vertically penetrate entire film thickness. Such feature maybe endow excellent transport behavior of charge carriers along them, since the transport and transfer of charge carriers do so without traversing any grain boundaries in this case [4, 41]. By comparison, interfacial microstructure of these two films differs obviously. For the CsPbIBr₂ film deposited on FTO/TiO₂ substrate without loading PEAI species, the interface between CsPbIBr₂ film and FTO/TiO₂ substrate is contacted seamlessly. However, there are many voids that have the typical size of ~100 nm in the same interface, in terms of CsPbIBr₂ film deposited on FTO/TiO₂ substrate loaded with PEAI species. These voids give rise to the rough contact interface between CsPbIBr₂ film and FTO/TiO₂ substrate. It is also noted that because PEAI species are sublimated during the thermal annealing stage of CsPbIBr₂ film, we conclude that the pre-deposited PEAI species likely act as pore-forming agent in the present case. The strategy of using pore-forming agent has been widely used to create pores in traditional ceramic materials [44, 45]. Our viewpoint can be further supported by the cross section SEM image of the same CsPbIBr₂ film prepared with large concentration of PEAI solution (10 mg mL⁻¹), as provided in Fig. S7. It is clear that the voids with much larger sizes are produced when the more PEAI species were pre-deposited. Overall, the PEAI species on FTO/TiO₂ substrate, serving as pore-forming agent, can promote the formation of large-sized grains in ultimate CsPbIBr₂ film as well as some voids at the interface between CsPbIBr₂ film and FTO/TiO₂ substrate.

3.3 Crystalline and Optical Property Analysis

Next, the crystalline structure and optical properties of as-prepared CsPbIBr₂ films are investigated. For clarification, the CsPbIBr₂ film as well the cell deposited on FTO/TiO₂ substrate without loading of PEAI species are labeled as “without void,” and the ones on FTO/TiO₂ substrate with

loading of PEAI species are named as “with voids” herein after. Figure 3a presents X-ray diffraction (XRD) patterns of CsPbIBr₂ films without and with interfacial voids. Both samples exhibit the pure cubic perovskite phase, since the diffraction peaks at 15.1°, 21.4°, 26.6°, 30.4°, 33.8°, and 37.8° are well consistent with those of (100), (110), (111), (200), (210), and (211) planes of CsPbIBr₂ crystals reported previously [10, 26]. Meanwhile, the XRD peaks of (100) and (200) planes are dominantly intense for both samples, indicating that the grains in them have (100)-preferential orientation. For cubic perovskite polycrystalline films, {100} grains facets are generally along the direction perpendicular to FTO/TiO₂ substrate, which well coincides the vertically penetrated grains morphology observed in the cross section SEM images in Figs. 2c, d and S6 for the concerned CsPbIBr₂ films. In addition, the dominant diffraction peaks of CsPbIBr₂ film with interfacial voids are more intense than the one without voids, and the full-width-at-half-maximum (FWHM) values of its (100) and (200) XRD peaks are smaller (Table S1). These results reveal the better crystallinity with fewer intragranular defects and less scattering of grain boundaries for the CsPbIBr₂ film with interfacial voids, in consideration of the similar thickness of the two films [22, 41, 43]. Such features are in accordance with the larger grains of CsPbIBr₂ film with interfacial voids.

Figure 3b presents the ultraviolet–visible (UV–vis) spectra of as-prepared CsPbIBr₂ films. Both of them exhibit the typical absorption features of CsPbIBr₂ materials including the exciton absorption peak at ~560 nm and absorption edge of ~599 nm that is in accordance with the bandgap of CsPbIBr₂ (2.07 eV) [20, 25, 27]. In comparison, the CsPbIBr₂ film with interfacial voids shows higher absorption intensities in the whole absorption ranges, revealing its better light absorption capacity. In principle, this desired feature mainly originates from either improved quality of CsPbIBr₂ film or scattering effect of interfacial voids in it, in view of the similar thickness of the two films. To exclude the effect of the former, UV–vis characters of the concerned CsPbIBr₂ films were collected from the side of FTO glass, wherein the detection beam streams from the top surface of CsPbIBr₂ films. The results in Fig. S8 reveal that the differences of their absorption intensities decrease accordingly. That is to say, the better absorption ability of CsPbIBr₂ film with interfacial voids observed in Fig. 3b largely comes from the beneficial scattering effect of interfacial voids, which may make great contribution to J_{sc} of ultimate PSC.

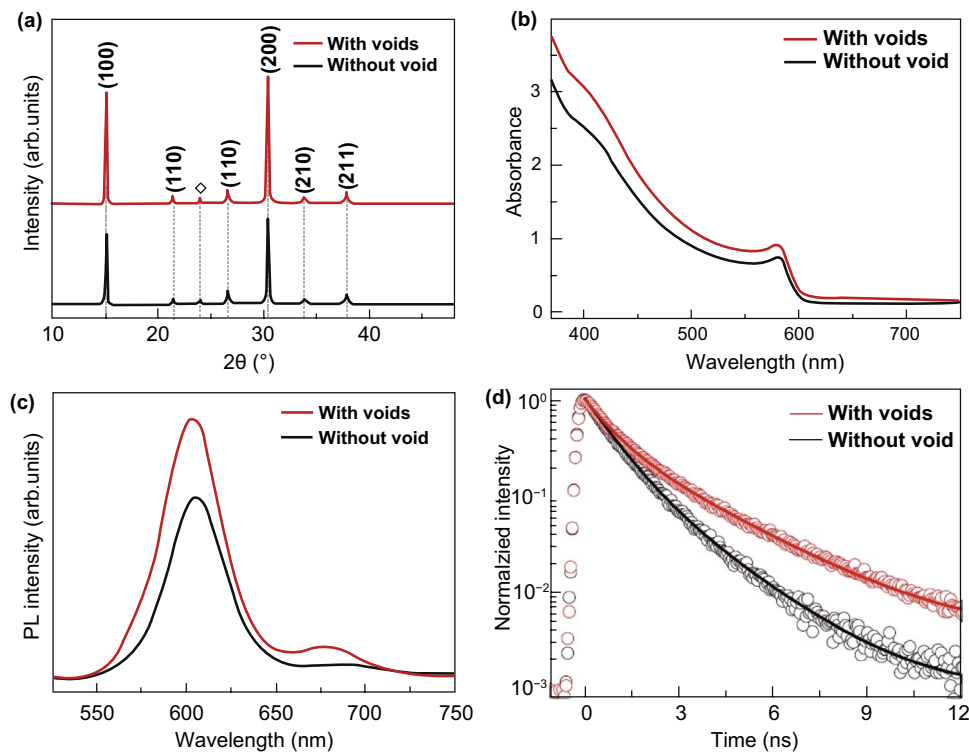


Fig. 3 **a** XRD patterns and **b** UV-vis absorption spectra of CsPbIBr₂ films without and with interfacial voids, **c** steady-state PL spectra and **d** TRPL curves of CsPbIBr₂ films without and with interfacial voids on insulating glass substrates instead of FTO/TiO₂ substrates

Figure 3c, d gives steady-state photoluminescence (PL) spectra and time-resolved PL (TRPL) curves of CsPbIBr₂ films without and with interfacial voids grown on insulating glass substrates instead of FTO/TiO₂ substrates, respectively. As shown in Fig. 3c, CsPbIBr₂ films exhibit the dominant PL peaks at ~600 nm, in well agreement with their bandgaps. The shoulder peaks can be also observed for both samples, as indicated by the logarithmic-scale PL plots in Fig. S9. This phenomenon is mainly caused by light-induced halide phase segregation in CsPbIBr₂ films, wherein some I-rich domains with low bandgap and Br-rich domains with wide bandgap are formed under illumination, as demonstrated in previous works [19, 46–48]. In addition, the CsPbIBr₂ film with interfacial voids yields the stronger PL peak intensity, revealing the weaker non-radiative recombination of charge carriers in it. Figure 3d shows the corresponding TRPL results, which can provide semi-quantitative information about non-radiative recombination of charge carriers [2, 4, 9, 48]. The curves are fitted by a bi-exponential decay function of time (t) [2, 4]: $F(t) = \sum A_i e^{-t/\tau_i}$; $i = 1, 2$, in which A_i and τ_i are weight factor and time constant, respectively. In this manner, the average carrier lifetime (t_{ave}) can be estimated

according to the equation of $\tau_{\text{ave}} = \sum A_i \tau_i^2 / \sum A_i \tau_i$; $i = 1, 2$. The CsPbIBr₂ film with interfacial voids exhibits the τ_{ave} of 1.91 ns, which is higher than the one without interfacial voids (1.26 ns). The longer τ_{ave} of the former indicates the fewer defects in it, which is originally attributed to the larger grains and better crystallinity of CsPbIBr₂ film with interfacial voids.

3.4 Photovoltaic Performance

Hitherto, we reveal that the CsPbIBr₂ film with interfacial voids has slightly larger grains and higher crystallinity, which result in the weaker non-radiative recombination of charge carriers in it. Such feature is expected to improve the V_{oc} and FF of ultimate PSC [18, 30, 32, 49]. Meanwhile, the interfacial voids trigger intense light scattering effect [50], which gives rise to the much higher absorption of the CsPbIBr₂ film and hence maybe boost the J_{sc} of corresponding PSC. It is generally recognized that interfacial voids are harmful to the performance of planar PSC, since

they inevitably reduce the contact area between absorber film and charge transporting layer, thus increasing the transporting resistance of charge carriers. Even so, in the present case, we speculate that such negative effect can be fully counteracted by the multiply beneficial contributions of the interfacial voids described above. To verify our inference, the CsPbI₂Br₂ films without and with interfacial voids are used to construct carbon-based, all-inorganic PSCs with the structure of FTO/TiO₂/CsPbI₂Br₂/Carbon as illustrated in Fig. 4a. Firstly, the PEAI solution concentration was optimized according to the performance of resulting PSCs. As shown in Fig. 4b, the PSC yields the optimized PCE when 3 mg mL⁻¹ PEAI solution was used. So, this solution is

adopted to fabricate all the PSCs hereinafter. Figure 4c provides the statistical PCEs of 20 independent PSCs based on the CsPbI₂Br₂ films without and with interfacial voids, which were measured under simulated AM 1.5 G illumination (100 mW cm⁻²) and a scan rate of 10 mV s⁻¹. A black mask containing a circular aperture with specific area of 0.085 cm² was used to confine the active area of the PSCs. Accordingly, the average PCEs are estimated to be 5.22 ± 0.54% and 9.54 ± 0.59% for the PSCs fabricated with CsPbI₂Br₂ films without and with interfacial voids, respectively. It is extremely surprised that the CsPbI₂Br₂ films with interfacial voids can enable over 85% enhancement in average PCE of carbon-based, all-inorganic PSCs. Figure 4d shows the

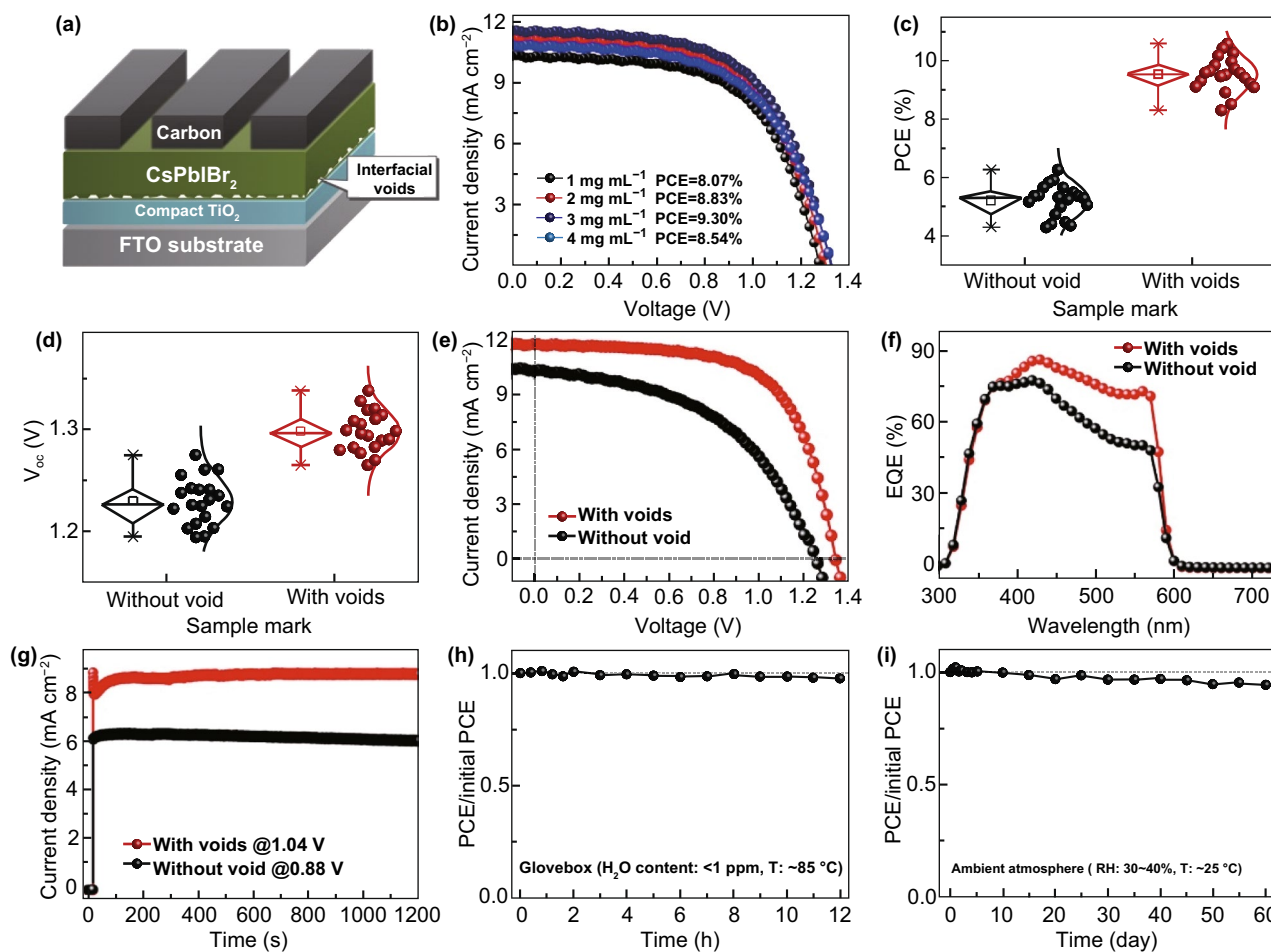


Fig. 4 **a** Schematic layer stacking of carbon-based, all-inorganic CsPbI₂Br₂ PSC, **b** typical *J*-*V* curves of the PSCs employed CsPbI₂Br₂ films prepared with different concentrations of PEAI solutions, **c** statistic PCEs and **d** *V*_{oc} distributions of 20 independent PSCs based on CsPbI₂Br₂ films without and with interfacial voids, **e** *J*-*V* curves, **f** EQE spectra, and **g** steady-state photocurrent outputs of the champion PSCs based on CsPbI₂Br₂ films without and with interfacial voids. Time-dependent variations of PCEs of the un-encapsulated PSC based on CsPbI₂Br₂ film with interfacial voids in **h** glovebox atmosphere and **i** ambient condition

statistical V_{oc} values of as-fabricated PSCs, from which the average V_{oc} values are estimated to be 1.230 ± 0.023 and 1.297 ± 0.018 V for the PSCs based on CsPbIBr₂ films without and with interfacial voids, respectively. Thus, we can conclude that the V_{oc} values of the PSCs based on CsPbIBr₂ films with interfacial voids are larger consistently. It is worth noting that the superior V_{oc} is not only vital to overcome the PCE obstacle facing current CsPbIBr₂ PSCs, but also can promote their applications in other energy conversion systems, such as water splitting cells [11, 17, 28].

Figure 4e displays the current density versus voltages (J - V) curves of the best-performing PSCs employed CsPbIBr₂ films without and with interfacial voids, respectively. The typical photovoltaic parameters including V_{oc} , FF, J_{sc} , and PCE are provided in Table 1. The

Table 1 Photovoltaic parameters of best-performing PSCs based on CsPbIBr₂ films without and with interfacial voids

Cells	V_{oc} (V)	FF	J_{sc} (mA cm ⁻²)	PCE (%)
Without void	1.254	0.49	10.31	6.34
With voids	1.338	0.65	11.73	10.20

PSC fabricated with CsPbIBr₂ film with interfacial voids delivers the V_{oc} of 1.338 V, FF of 0.65, and J_{sc} of 11.73 mA cm⁻², leading to a much higher PCE of 10.20%. Such PCE is beyond nearly all the CsPbIBr₂ PSCs reported previously. More importantly, as shown in Table 2, the V_{oc} achieved herein stands the highest value among them [8, 17–20, 25–27, 30, 31, 35, 47, 48, 51–56].

External quantum efficiency (EQE) spectra of the champion PSCs are given in Fig. 4f. Photocurrent response of each PSC is consistent with the absorption feature of CsPbIBr₂ film. By contrast, the PSC based on CsPbIBr₂ film with interfacial voids exhibits much higher EQEs in the wavelength regions from 400 to 580 nm, disclosing its better photoelectric conversion capability as a result of higher light absorption and more energetic extraction of charge carriers. Moreover, a remarkable EQE peak of 86% can be realized in the PSC. In addition, the integrated current densities from the EQE spectra (Fig. S10) are basically consistent with the J_{sc} provided in Table 1, wherein the discrepancies may be resulted from the absence of light soaking during EQE tests and the spectral mismatch [30, 31, 52].

Table 2 Summary of V_{oc} values and PCEs for CsPbIBr₂ PSCs reported so far

Cell configuration	E_g (eV)	V_{oc} (V)	PCE (%)	Refs.
FTO/c-TiO ₂ /CsPbIBr ₂ /Carbon	2.07	1.338	10.20	This work
FTO/TiO ₂ /SmBr ₃ /Sm-doped CsPbIBr ₂ /spiro-OMeTAD/Au	2.11	1.17	10.88	[30]
FTO/c-TiO ₂ /CsBr/CsPbIBr ₂ /Carbon	2.05	1.261	10.71	[18]
FTO/TiO ₂ /CsPb(Ba)IBr ₂ /spiro-OMeTAD/Au	~2.11	1.19	10.51	[31]
ITO/SnO ₂ /S-doped CsPbIBr ₂ /P3HT/Au	2.05	1.30	9.78	[25]
FTO/c-TiO ₂ /CsPbIBr ₂ /Carbon	2.05	1.245	9.16	[19]
FTO/c-TiO ₂ /CsPbIBr ₂ /Carbon	2.05	1.283	8.60	[51]
ITO/SnO ₂ /CsPbIBr ₂ /spiro-OMeTAD/Ag	2.00	1.15	8.54	[52]
FTO/c-TiO ₂ /m-TiO ₂ /CsPbIBr ₂ /Carbon	1.90	1.08	8.25	[8]
FTO/c-TiO ₂ /CsPbIBr ₂ /spiro-OMeTAD/Au	2.05	1.227	8.02	[47]
ITO/SnO ₂ /C60/CsPbIBr ₂ /spiro-OMeTAD/Au	2.04	1.18	7.34	[48]
FTO/TiO ₂ /CsPbIBr ₂ /spiro-OMeTAD/Ag	2.07	1.28	7.31	[53]
ITO/Passivated SnO ₂ /CsPbIBr ₂ /Carbon	2.07	1.23	7.00	[17]
FTO/c-TiO ₂ /CsPbIBr ₂ /Carbon	2.05	1.142	6.55	[19]
FTO/c-TiO ₂ /m-TiO ₂ /CsPbIBr ₂ /spiro-OMeTAD/Au	2.05	1.121	6.30	[54]
FTO/c-TiO ₂ /m-TiO ₂ /CsPbIBr ₂ /Carbon	1.89	0.96	6.14	[20]
FTO/In ₂ S ₃ /CsPbIBr ₂ /Spiro-OMeTAD/Ag	2.08	1.09	5.59	[27]
FTO/NiO _x /CsPbIBr ₂ /ZnO/Al	2.10	1.01	5.57	[26]
FTO/NiO _x /CsPbIBr ₂ /MoO _x /Au	2.08	0.85	5.52	[35]
ITO/ZnO/CsPbIBr ₂ /spiro-OMeTAD/Ag	2.06	1.04	4.8	[55]
FTO/c-TiO ₂ /CsPbIBr ₂ /Au	2.05	0.959	4.70	[56]



We also tested the steady-state photocurrent outputs of the champion PSCs under maximum power-point conditions (Fig. 4g). They exhibit fast light-response, indicating smooth charge extraction. This desired character is mainly relied to large energy difference of conduction band minimums (CBMs) for CsPbIBr₂ absorber and TiO₂ ETL [18, 51]. One can see that the PSC based on CsPbIBr₂ film without interfacial voids yields the stabilized current density of $\sim 6.18 \text{ mA cm}^{-2}$ under a constant bias voltage of 0.880 V, which corresponds to a stabilized PCE of 5.44%. And, the one without interfacial voids exhibits the stabilized PCE of 8.99% under 1.040 V, which supports the better performance of the PSC fabricated with CsPbIBr₂ film with interfacial voids. However, both steady-state PCEs are smaller than those of extracted from J - V curves, indicative of inevitable anomalous J - V hysteresis. The J - V hysteresis is frequently observed in previous CsPbIBr₂ PSCs and primarily related to light-induced phase segregation in CsPbIBr₂ films [8, 46–48, 51, 52, 54, 55]. In addition, one can notice that during the test period the photocurrent outputs of both PSCs are stable in ambient atmosphere, revealing their excellent ability against humidity and light attacking.

Finally, thermal stability and long-term stability of the champion PSC prepared with CsPbIBr₂ film with interfacial voids were studied. For thermal stability test, the un-encapsulated PSC was continuously heated at 85 °C on a hotplate in N₂-filled glovebox. And, for long-term stability test the same PSC was stored at room temperature in ambient atmosphere with relative humidity of 30–40%. As shown in Fig. 4h, the PSC can remain $\sim 97\%$ of its initial PCE after being tested for 12 h, indicative of its superior thermal stability. We attribute this favored aspect to the excellent resistance of CsPbIBr₂ film to high temperature, as it is prepared at a higher annealing temperature of 280 °C. In general, the annealing temperatures for its analogs including CsPbI₃, CsPbI₂Br, and CsPbBr₃ are 200, 160, and 250 °C, respectively. Figure 4i provides the result of long-term stability test. The same PSC can sustain $\sim 94\%$ of its initial PCE after storing for 60 days, making clear its superior long-term stability against humidity and interface degradation. Overall, one can conclude that the CsPbIBr₂ film with interfacial voids can enable the carbon-based, all-inorganic PSC with outstanding PCE and record-high V_{oc} , along with excellent operation stability under light, thermal, or humidity stress.

3.5 Carrier Dynamics

To gain insight into the relationship between the carrier dynamics and performance of PSCs prepared with CsPbIBr₂ films without and with interfacial voids, we explored the transport mechanisms in the fabricated PSCs by means of various characterization techniques, including dark J - V , light-intensity-dependent V_{oc} , transient photocurrent (TPC), transient photovoltage (TPV), electrochemical impedance spectroscopy (EIS), and Mott–Schottky (M–S) measurements. Figure 5a gives the dark J - V curves of investigated PSCs. In general, the dark J - V curve of a solar cell is dominated by the diode law. Based on it, the J_0 can be estimated from the intercept at zero voltage of the linear regression from semi-logarithmic J - V plot in the region close to the diode turn-on voltage [19, 23, 57]. In general, J_0 is governed by recombination of charge carriers in the cell, wherein a low J_0 is always accompanied by the suppressed recombination. Herein, we can see that the PSC based on CsPbIBr₂ film with interfacial voids exhibits much smaller J_0 ($1.14 \times 10^{-7} \text{ mA cm}^{-2}$) than the one without interfacial voids ($1.37 \times 10^{-5} \text{ mA cm}^{-2}$), indicating the weaker recombination of charge carriers in it. It should be noted that although the larger grains and higher crystallinity can partly decrease J_0 of the PSC based on CsPbIBr₂ film with interfacial voids, we believe that the interfacial voids may dominantly contribute to its much smaller J_0 . This is because the PSC exhibits the similarly lower dark current under high bias voltages such as 1.5 V.

Figure 5b presents the plots of V_{oc} as a function of incident light intensity for the concerned PSCs. One can see that the V_{oc} improves with the logarithmic light intensity monotonically, revealing the dominant trap-assisted Shockley–Read–Hall recombination in both PSCs [9, 23, 30, 31]. In addition, the PSC based on CsPbIBr₂ film without interfacial void shows a slope of $2.08 k_B T/q$, while the one with voids yields a smaller slope of $1.70 k_B T/q$ that is more close to $1 k_B T/q$, where q is the electric charge, T is temperature, and k_B is the Boltzmann constant. These results further confirm that the recombination of charge carriers has been greatly suppressed in the PSC based on CsPbIBr₂ film with interfacial voids.

Figure 5c gives the TPC curves of the corresponding PSCs, which can reflect the extraction and transport properties of charge carriers. The photocurrent decay constants are estimated to be 2.64 and 1.83 μs for the PSCs based on

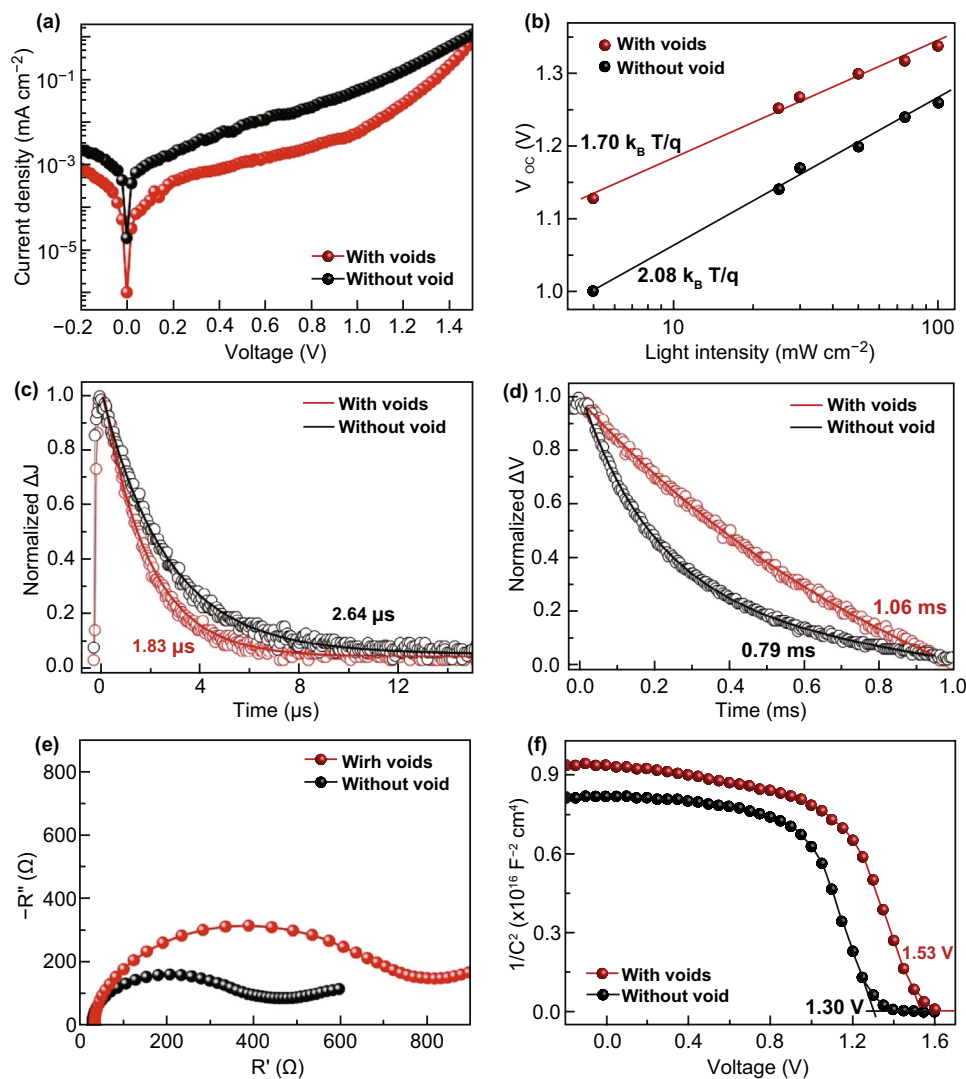


Fig. 5 **a** Dark J - V curves, **b** the dependence of V_{oc} on light intensity, **c** TPC curves, and **d** TPV curves for the PSCs based on CsPbIBr₂ films without and with interfacial voids, **e** Nyquist plots and **f** M-S plots of the same cells

CsPbIBr₂ film without and with interfacial voids, respectively. These results mean that the interfacial voids do not damage the extraction and transport of charge carriers [18, 19, 51], even though they induce significantly decreased dark current density. Instead, the extraction and transport of charge carriers are improved slightly, which probably benefit from the larger grains and higher crystallinity of CsPbIBr₂ film with interfacial voids that endow its better transport ability for photon-generated carriers. At the same time, the recombination of charge carriers in the PSCs is monitored by TPV measurements [18, 19, 51]. The results in Fig. 5d indicate that the PSC based on CsPbIBr₂ film with interfacial voids has the slower photovoltage decay (1.06 ms) than the

one without interfacial void (0.79 ms), which supports the suppressed recombination of charge carriers in the former again.

Furthermore, EIS tests were performed on the fabricated PSCs to estimate recombination resistance (R_{rec}) of charge carriers in them [14, 17, 25]. The Nyquist plots that were recorded at a forward bias voltage of 1.0 V under dark condition are given in Fig. 5e. The clear arc is involved to carrier recombination, reflecting the recombination resistance R_{rec} . The larger R_{rec} of the PSC based on CsPbIBr₂ film with interfacial voids is well accordance with the suppressed recombination of charge carriers in it. On the other hand, the M-S results in Fig. 5f indicate that the built-in potential (V_{bi})

of the PSC based on CsPbIBr₂ film with interfacial voids is 1.56 V, which is much higher than that of the one without interfacial void ($V_{bi} = 1.30$ V). A larger V_{bi} not only provide higher driving force to dissociate photo-generated carriers, but also contribute to form a wider depletion region for suppressing recombination of charge carriers in the PSC, as verified by the dark $J-V$, TPV, and EIS results above [15, 18, 30, 31]. As a whole, the higher V_{bi} and weaker recombination of charge carriers directly contributes to the record-high V_{oc} as well as superior FF of the PSC based on CsPbIBr₂ film with interfacial voids. And, the higher absorption of CsPbIBr₂ film as a result of intense light scattering effect of interfacial voids gives rise to its higher J_{sc} . Therefore, the PCE of the PSC based on CsPbIBr₂ film with interfacial voids is improved significantly.

4 Conclusions

We demonstrate a new interfacial engineering for carbon-based, inorganic CsPbIBr₂ PSC by manufacturing interfacial voids between TiO₂ ETL and CsPbIBr₂ film. The interfacial voids contribute to better absorption, higher V_{bi} , and smaller J_0 of the PSC, as results of enhanced light scattering in CsPbIBr₂ film, boosted crystal quality of CsPbIBr₂ grains, and significant suppressed recombination of charge carriers. Consequently, the optimized PSC achieves the PCE of as high as 10.20% coupled with the V_{oc} of 1.338 V. Such V_{oc} represents the best value among CsPbIBr₂ PSCs reported earlier. More promisingly, the non-encapsulated PSC can remain ~97% and ~94% of its initial PCE after being heated at 85 °C for 12 h or storing in ambient atmosphere with relative humidity of 30–40% for 60 days, respectively, suggesting its excellent stability against light, thermal, and humidity stresses.

Acknowledgements All the authors gratefully acknowledge the financial support from the National Natural Science Foundation of China (Nos. 61804113, 61874083), Initiative Postdocs Supporting Program (BX20190261), the National Natural Science Foundation of Shaanxi Province (2018ZDCXL-GY-08-02-02 and 2017JM6049), and the Fundamental Research Funds for the Central Universities (JB181107 and JBX171103).

Open Access This article is licensed under a Creative Commons Attribution 4.0 International License, which permits use, sharing, adaptation, distribution and reproduction in any medium or format, as long as you give appropriate credit to the original author(s) and

the source, provide a link to the Creative Commons licence, and indicate if changes were made. The images or other third party material in this article are included in the article's Creative Commons licence, unless indicated otherwise in a credit line to the material. If material is not included in the article's Creative Commons licence and your intended use is not permitted by statutory regulation or exceeds the permitted use, you will need to obtain permission directly from the copyright holder. To view a copy of this licence, visit <http://creativecommons.org/licenses/by/4.0/>.

Electronic supplementary material The online version of this article (<https://doi.org/10.1007/s40820-020-00425-1>) contains supplementary material, which is available to authorized users.

References

1. A. Kojima, K. Teshima, Y. Shirai, T. Miyasaka, Organometal halide perovskites as visible-light sensitizers for photovoltaic cells. *J. Am. Chem. Soc.* **131**, 6050–6051 (2009). <https://doi.org/10.1021/ja809598r>
2. H.S. Jung, N.G. Park, Perovskite solar cells: from materials to devices. *Small* **11**, 10–25 (2015). <https://doi.org/10.1002/sml.201402767>
3. Y. Rong, Y. Hu, A. Mei, H. Tan, M.I. Saidaminov et al., Challenges for commercializing perovskite solar cells. *Science* **361**, eaat8235 (2018). <https://doi.org/10.1126/science.aat8235>
4. M. Saliba, J.P. Correa-Baena, M. Grätzel, A. Hagfeldt, A. Abate, Perovskite solar cells: from the atomic level to film quality and device performance. *Angew. Chem. Int. Ed.* **57**, 2554–2569 (2018). <https://doi.org/10.1002/anie.201703226>
5. Cell efficiency chart. <https://www.nrel.gov/pv/cell-efficiency.html>. Accessed: Aug 2019
6. C.C. Boyd, R. Cheacharoen, T. Leijtens, M.D. McGehee, Understanding degradation mechanisms and improving stability of perovskite photovoltaics. *Chem. Rev.* **119**, 3418–3451 (2019). <https://doi.org/10.1021/acs.chemrev.8b00336>
7. J. Liang, C. Wang, Y. Wang, Z. Xu, Z. Lu et al., All-inorganic perovskite solar cells. *J. Am. Chem. Soc.* **138**, 15829–15832 (2016). <https://doi.org/10.1021/jacs.6b10227>
8. J. Liang, P. Zhao, C. Wang, Y. Wang, Y. Hu, G. Zhu, L. Ma, J. Liu, Z. Jin, CsPb_{0.9}Sn_{0.1}IBr₂ based all-inorganic perovskite solar cells with exceptional efficiency and stability. *J. Am. Chem. Soc.* **139**, 14009–14012 (2017). <https://doi.org/10.1021/jacs.7b07949>
9. J. Duan, Y. Zhao, B. He, Q. Tang, High-purity inorganic perovskite films for solar cells with 9.72% efficiency. *Angew. Chem. Int. Ed.* **57**, 3787–3791 (2018). <https://doi.org/10.1002/anie.201800019>
10. J. Zhang, G. Hodes, Z. Jin, S. Liu, All-inorganic CsPbX₃ perovskite solar cells: progress and prospects. *Angew. Chem. Int. Ed.* **58**, 15596–15618 (2019). <https://doi.org/10.1002/anie.201901081>

11. A. Ho-Baillie, M. Zhang, C.F.J. Lau, F.-J. Ma, S. Huang, Untapped potentials of inorganic metal halide perovskite solar cells. *Joule* **3**, 938–955 (2019). <https://doi.org/10.1016/j.joule.2019.02.002>
12. S. Xiang, Z. Fu, W. Li, Y. Wei, J. Liu et al., Highly air-stable carbon-based α -CsPbI₃ perovskite solar cells with a broadened optical spectrum. *ACS Energy Lett.* **3**, 1824–1831 (2018). <https://doi.org/10.1021/acsenergylett.8b00820>
13. S. Xiang, W. Li, Y. Wei, J. Liu, H. Liu, L. Zhu, S. Yang, H. Chen, Sodium doping pushes the efficiency of carbon-based CsPbI₃ perovskite solar cells to 10.7%. *iScience* **15**, 156 (2019). <https://doi.org/10.1016/j.isci.2019.04.025>
14. X. Zhang, Y. Zhou, Y. Li, J. Sun, X. Lu et al., Efficient and carbon-based hole transport layer-free CsPbI₂Br planar perovskite solar cells using PMMA modification. *J. Mater. Chem. C* **7**, 3852–3861 (2019). <https://doi.org/10.1039/C9TC00374F>
15. Y. Guo, F. Zhao, J. Tao, J. Jiang, J. Zhang, J. Yang, Z. Hu, J. Chu, Efficient and hole-transporting-layer-free CsPbI₂Br planar heterojunction perovskite solar cells through rubidium passivation. *ChemSusChem* **12**, 983–989 (2019). <https://doi.org/10.1002/cssc.201802690>
16. X. Meng, Z. Wang, W. Qian, Z. Zhu, T. Zhang et al., Excess cesium iodide induces spinodal decomposition of CsPbI₂Br perovskite films. *J. Phys. Chem. Lett.* **10**, 194–199 (2019). <https://doi.org/10.1021/acs.jpcclett.8b03742>
17. Z. Guo, S. Teo, Z. Xu, C. Zhang, Y. Kamata, S. Hayase, T. Ma, Achievable high V_{oc} of carbon based all-inorganic CsPbIBr₂ perovskite solar cells through interface engineering. *J. Mater. Chem. A* **7**, 1227–1232 (2019). <https://doi.org/10.1039/C8TA09838G>
18. W. Zhu, Z. Zhang, W. Chai, Q. Zhang, D. Chen et al., Band alignment engineering towards 10.71%-efficiency carbon-based, all-inorganic planar CsPbIBr₂ perovskite solar cells. *ChemSusChem* **12**, 2318 (2019). <https://doi.org/10.1002/cssc.201900611>
19. W. Zhu, Q. Zhang, C. Zhang, Z. Zhang, D. Chen, Z. Lin, J. Chang, J. Zhang, Y. Hao, Aged precursor solution toward low-temperature fabrication of efficient carbon-based all-inorganic planar CsPbIBr₂ perovskite solar cells. *ACS Appl. Energy Mater.* **1**, 4991–4997 (2018). <https://doi.org/10.1021/acsaem.8b00972>
20. J. Liang, Z. Liu, L. Qiu, Z. Hawash, L. Meng et al., Enhancing optical, electronic, crystalline, and morphological properties of cesium lead halide by Mn substitution for high-stability all-inorganic perovskite solar cells with carbon electrodes. *Adv. Energy Mater.* **8**, 1800504 (2018). <https://doi.org/10.1002/aenm.201800504>
21. X. Liu, X. Tan, Z. Liu, H. Ye, B. Sun, T. Shi, Z. Tang, G. Liao, Boosting the efficiency of carbon-based planar CsPbBr₃ perovskite solar cells by a modified multistep spin-coating technique and interface engineering. *Nano Energy* **56**, 184–195 (2019). <https://doi.org/10.1016/j.nanoen.2018.11.053>
22. J. Liu, L. Zhu, S. Xiang, Y. Wei, M. Xie, H. Liu, W. Li, H. Chen, Growing high-quality CsPbBr₃ by using porous CsPb₂Br₅ as an intermediate: a promising light absorber in carbon-based perovskite solar cells. *Sustain. Energy Fuels* **3**, 184–194 (2019). <https://doi.org/10.1039/C8SE00442K>
23. J. Duan, Y. Zhao, X. Yang, Y. Wang, B. He, Q. Tang, Lanthanide ions doped CsPbBr₃ halides for HTM-free 10.14%-efficiency inorganic perovskite solar cell with an ultrahigh open-circuit voltage of 1.594 V. *Adv. Energy Mater.* **8**, 1802346 (2018). <https://doi.org/10.1002/aenm.201802346>
24. Y. Zhou, Y. Zhao, Chemical stability and instability of inorganic halide perovskites. *Energy Environ. Sci.* **12**, 1495 (2019). <https://doi.org/10.1039/C8EE03559H>
25. Z. Wang, A.K. Baranwal, M.A. Kamarudin, C.H. Ng, M. Pandey, T. Ma, S. Hayase, Xanthate-induced sulfur doped all-inorganic perovskite with superior phase stability and enhanced performance. *Nano Energy* **59**, 258–267 (2019). <https://doi.org/10.1016/j.nanoen.2019.02.049>
26. J. Lin, M. Lai, L. Dou, C.S. Kley, H. Chen et al., Thermochromic halide perovskite solar cells. *Nat. Mater.* **17**, 261 (2018). <https://doi.org/10.1038/s41563-017-0006-0>
27. B. Yang, M. Wang, X. Hu, T. Zhou, Z. Zang, Highly efficient semitransparent CsPbIBr₂ perovskite solar cells via low-temperature processed In₂S₃ as electron-transport-layer. *Nano Energy* **57**, 718–727 (2019). <https://doi.org/10.1016/j.nanoen.2018.12.097>
28. M. Moniruddin, B. Ilyassov, X. Zhao, E. Smith, T. Serikov, N. Ibrayev, R. Asmatulu, N. Nuraje, Recent progress on perovskite materials in photovoltaic and water splitting applications. *Mater. Today Energy* **7**, 246–259 (2018). <https://doi.org/10.1016/j.mtener.2017.10.005>
29. F. Meillaud, A. Shah, C. Droz, E. Vallat-Sauvain, C. Miazza, Efficiency limits for single-junction and tandem solar cells. *Sol. Energy Mater. Sol. Cells* **90**, 2952–2959 (2006). <https://doi.org/10.1016/j.solmat.2006.06.002>
30. W.S. Subhani, K. Wang, M. Du, X. Wang, S. Liu, Interface-modification-induced gradient energy band for highly efficient CsPbIBr₂ perovskite solar cells. *Adv. Energy Mater.* (2019). <https://doi.org/10.1002/aenm.201803785>
31. W.S. Subhani, K. Wang, M. Du, S.F. Liu, Gold Schmidt-rule-deviated perovskite CsPbIBr₂ by barium substitution for efficient solar cells. *Nano Energy* **61**, 165–172 (2019). <https://doi.org/10.1016/j.nanoen.2019.04.066>
32. F. Meng, A. Liu, L. Gao, J. Cao, Y. Yan et al., Current progress in interfacial engineering of carbon-based perovskite solar cells. *J. Mater. Chem. A* **7**, 8690–8699 (2019). <https://doi.org/10.1039/C9TA01364D>
33. D.B. Khadka, Y. Shirai, M. Yanagida, K. Miyano, Degradation of encapsulated perovskite solar cells driven by deep trap states and interfacial deterioration. *J. Mater. Chem. C* **6**, 162–170 (2018). <https://doi.org/10.1039/C7TC03733C>
34. B. Roose, Q. Wang, A. Abate, The role of charge selective contacts in perovskite solar cell stability. *Adv. Energy Mater.* **9**, 1803140 (2019). <https://doi.org/10.1002/aenm.201803140>
35. C. Liu, W. Li, J. Chen, J. Fan, Y. Mai, R.E. Schropp, Ultrathin MoO_x as cathode buffer layer for the improvement of all-inorganic CsPbIBr₂ perovskite solar cells. *Nano Energy* **41**, 75–83 (2017). <https://doi.org/10.1016/j.nanoen.2017.08.048>



36. C. Bao, J. Yang, S. Bai, W. Xu, Z. Yan et al., High performance and stable all-inorganic metal halide perovskite-based photodetectors for optical communication applications. *Adv. Mater.* **30**, 1803422 (2018). <https://doi.org/10.1002/adma.201803422>
37. Q. Jiang, Y. Zhao, X. Zhang, X. Yang, Y. Chen et al., Surface passivation of perovskite film for efficient solar cells. *Nat. Photonics* **13**, 460–466 (2019). <https://doi.org/10.1038/s41566-019-0398-2>
38. Y. Wang, T. Zhang, M. Kan, Y. Zhao, Bifunctional stabilization of all-inorganic α -CsPbI₃ perovskite for 17% efficiency photovoltaics. *J. Am. Chem. Soc.* **140**, 12345–12348 (2018). <https://doi.org/10.1021/jacs.8b07927>
39. A. Dualeh, P. Gao, S.I. Seok, M.K. Nazeeruddin, M. Grätzel, Thermal behavior of methylammonium lead-trihalide perovskite photovoltaic light harvesters. *Chem. Mater.* **26**, 6160–6164 (2014). <https://doi.org/10.1021/cm502468k>
40. N.N. Shlenskaya, N.A. Belich, M. Grätzel, E.A. Goodilin, A.B. Tarasov, Light-induced reactivity of gold and hybrid perovskite as a new possible degradation mechanism in perovskite solar cells. *J. Mater. Chem. A* **6**, 1780–1786 (2018). <https://doi.org/10.1039/C7TA10217H>
41. W. Zhu, C. Bao, B. Lv, F. Li, Y. Yi et al., Dramatically promoted crystallization control of organolead triiodide perovskite film by a homogeneous cap for high efficiency planar-heterojunction solar cells. *J. Mater. Chem. A* **4**, 12535–12542 (2016). <https://doi.org/10.1039/C6TA04332A>
42. G. Gottstein, A. King, L. Shvindlerman, The effect of triple-junction drag on grain growth. *Acta Mater.* **48**, 397–403 (2000). [https://doi.org/10.1016/S1359-6454\(99\)00373-0](https://doi.org/10.1016/S1359-6454(99)00373-0)
43. C. Bi, Q. Wang, Y. Shao, Y. Yuan, Z. Xiao, J. Huang, Non-wetting surface-driven high-aspect-ratio crystalline grain growth for efficient hybrid perovskite solar cells. *Nat. Commun.* **6**, 7747 (2015). <https://doi.org/10.1038/ncomms8747>
44. F. Chen, Q. Shen, F. Yan, L. Zhang, Pressureless sintering of α -Si₃N₄ porous ceramics using a H₃PO₄ pore-forming agent. *J. Am. Ceram. Soc.* **90**, 2379–2383 (2007). <https://doi.org/10.1111/j.1551-2916.2007.01800.x>
45. C. Galassi, Processing of porous ceramics: piezoelectric materials. *J. Eur. Ceram. Soc.* **26**, 2951–2958 (2006). <https://doi.org/10.1016/j.jeurceramsoc.2006.02.011>
46. D.J. Slotcavage, H.I. Karunadasa, M.D. McGehee, Light-induced phase segregation in halide-perovskite absorbers. *ACS Energy Lett.* **1**, 1199–1205 (2016). <https://doi.org/10.1021/acsenrgylett.6b00495>
47. W. Li, M.U. Rothmann, A. Liu, Z. Wang, Y. Zhang et al., Phase segregation enhanced ion movement in efficient inorganic CsPbIBr₂ solar cells. *Adv. Energy Mater.* **7**, 1700946 (2017). <https://doi.org/10.1002/aenm.201700946>
48. N. Li, Z. Zhu, J. Li, A.K.Y. Jen, L. Wang, Inorganic CsPb_{1-x}Sn_xIBr₂ for efficient wide-bandgap perovskite solar cells. *Adv. Energy Mater.* **8**, 1800525 (2018). <https://doi.org/10.1002/aenm.201800525>
49. I. Gelmetti, N. Montcada, A. Perez-Rodriguez, E. Barrena, C. Ocal et al., Energy alignment and recombination in perovskite solar cells: weighted influence on the open circuit voltage. *Energy Environ. Sci.* **12**, 1309–1316 (2019). <https://doi.org/10.1039/C9EE00528E>
50. S.M. Kang, S. Jang, J.K. Lee, J. Yoon, D.E. Yoo, J.W. Lee, M. Choi, N.G. Park, Moth-Eye TiO₂ layer for improving light harvesting efficiency in perovskite solar cells. *Small* **12**, 2443–2449 (2016). <https://doi.org/10.1002/smll.201600428>
51. Q. Zhang, W. Zhu, D. Chen, Z. Zhang, Z. Lin et al., Light processing enables efficient carbon-based, all-inorganic planar CsPbIBr₂ solar cells with high photovoltages. *ACS Appl. Mater. Interfaces* **11**, 2997–3005 (2018). <https://doi.org/10.1021/acsami.8b17839>
52. Y. Jiang, J. Yuan, Y. Ni, J. Yang, Y. Wang, T. Jiu, M. Yuan, J. Chen, Reduced-dimensional α -CsPbX₃ perovskites for efficient and stable photovoltaics. *Joule* **2**, 1356–1368 (2018). <https://doi.org/10.1016/j.joule.2018.05.004>
53. J. Lu, S.-C. Chen, Q. Zheng, Defect passivation of CsPbIBr₂ perovskites for high-performance solar cells with large open-circuit voltage of 1.28 V. *ACS Appl. Energy Mater.* **1**, 5872–5878 (2018). <https://doi.org/10.1021/acsaem.8b01430>
54. C.F.J. Lau, X. Deng, Q. Ma, J. Zheng, J.S. Yun, M.A. Green, S. Huang, A.W. Ho-Baillie, CsPbIBr₂ perovskite solar cell by spray-assisted deposition. *ACS Energy Lett.* **1**, 573–577 (2016). <https://doi.org/10.1021/acsenrgylett.6b00341>
55. M. Aamir, T. Adhikari, M. Sher, N. Revaprasadu, W. Khalid, J. Akhtar, J.-M. Nunzi, Fabrication of planar heterojunction CsPbBr₂I perovskite solar cells using ZnO as an electron transport layer and improved solar energy conversion efficiency. *New J. Chem.* **42**, 14104–14110 (2018). <https://doi.org/10.1039/C8NJ02238K>
56. Q. Ma, S. Huang, X. Wen, M.A. Green, A.W. Ho-Baillie, Hole transport layer free inorganic CsPbIBr₂ perovskite solar cell by dual source thermal evaporation. *Adv. Energy Mater.* **6**, 1502202 (2016). <https://doi.org/10.1002/aenm.201502202>
57. C. Li, Z. Song, D. Zhao, C. Xiao, B. Subedi et al., Reducing saturation-current density to realize high-efficiency low-bandgap mixed tin-lead halide perovskite solar cells. *Adv. Energy Mater.* **9**(3), 1803135 (2019). <https://doi.org/10.1002/aenm.201803135>